Communications Earth & Environment https://doi.org/10.1038/s43247-026-03339-9

Article in Press

Reversible copper coordination redirects pyrolysis products in waste polyurethane enamelled copper wire

Received: 15 May 2025

Accepted: 16 February 2026

Cite this article as: Zhang, W., Zhang, X., Geng, Y. *et al.* Reversible copper coordination redirects pyrolysis products in waste polyurethane enamelled copper wire. *Commun Earth Environ* (2026). https://doi.org/10.1038/s43247-026-03339-9

Wei Zhang, Xiaoguang Zhang, Yiqi Geng, Linbo Zhang, Ran Tao, Bin Li & Yufeng Wu

Reversible copper coordination redirects pyrolysis products in waste polyurethane enamelled copper wire

Wei Zhang[1], Xiaoguang Zhang[1], Yiqi Geng[2], Linbo Zhang[3], Tao Ran[1], Bin Li[1], Yufeng Wu[1*]

[1] State Key Laboratory of Materials Low-Carbon Recycling, Beijing University of Technology, Beijing, 100124, China.

[2] Institute of Bioresource and Agriculture, Department of Biology, Hong Kong Baptist University, Kowloon Tong 999077, Hong Kong Special Administrative Region of China.

[3] College of Materials Science and Engineering, Taiyuan University of Technology, Taiyuan, 030024, China.

*Corresponding author: Yufeng Wu

Email: wuyufeng3r@126.com

Tel: +86-10-67396234; Fax:+86-10-67396234

Abstract

Here we address a key mechanistic question that limits thermochemical upcycling of waste polyurethane wire: copper is not an inert background but actively redirects pyrolysis products. We propose a copper-assisted dynamic pyrolysis model in which copper reshapes the conversion-dependent energy-barrier profile through electronic-structure regulation, leading to a predictable shift in dominant reaction routes. Thermogravimetric analysis reveals a robust three-stage decomposition and a pronounced evolution of apparent barriers with conversion, consistent with a late-stage regime governed by radical reorganisation, condensation and char formation. Temperature-resolved product fingerprints provide direct chemical evidence for pathway selectivity. Reversible copper coordination and frontier-orbital interactions lower key transition barriers and stabilise intermediates, promoting radical recombination and aromatisation. These results establish a cross-scale link between macroscopic pyrolysis behaviour, barrier evolution and product selectivity, and offer a general framework for endogenous metal regulation, supporting cleaner processing and improved copper recovery.

Keywords: Waste polyurethane wire; Copper-assisted pyrolysis; Electronic-structure regulation; Density functional theory

Introduction

Copper is a critical material underpinning modern industrial systems, owing to its outstanding electrical conductivity, thermal conductivity, and ductility. These properties make it indispensable in emerging sectors such as renewable energy, electronic information technology, and high-end equipment manufacturing[1, 2]. The accelerating global energy transition has pronounced increased copper demand, as photovoltaic systems, electric vehicles, and charging infrastructure require substantially more copper than traditional applications[3, 4]. 20% to 40% by 2040. However, the global supply of copper ore remains limited, leading to an increasingly pronounced supply-demand imbalance. According to the International Energy Agency, the share of copper demand attributable to clean energy technologies is expected to rise from the current level in the coming decades[5, 6]. Waste enameled copper wires are typical examples of organic-copper containing composite waste materials. With the rapid advancement of science and technology, global demand for enameled wires has been increasing steadily, accompanied by a continuous rise in electronic waste generation[7-9]. The recycling and reuse of copper-containing waste enameled wires represent a vital strategy to address the growing imbalance between copper supply and demand[10, 11]. Enameled wires come in various types, featuring complex organic coatings and widespread applications across nearly all sectors of human activity. This paper focuses on polyurethane enameled wire, one of the most commonly used types. Due to its excellent performance, it is widely applied in industrial motors, precision electronics, instrumentation, and household appliances[12-14].

The recycling of waste enameled wires has traditionally focused on the recovery of metallic copper, while the treatment of the insulating coating remains technically challenging[15, 16]. Thermochemical deconstruction represents one of the most effective and primary strategies for the clean, homogeneous, and high-value utilization of waste polyurethane enameled wires. Among these approaches, oxygen-free pyrolysis offers pronounced advantages, including volume reduction, detoxification, and high resource recovery efficiency[17-24]. It enables the comprehensive recycling of all waste components, including precious metals and organic matter, making it a promising pathway toward carbon neutrality. With the continuous advancement of pyrolysis

research, traditional solid-phase pyrolysis systems have become insufficient to meet the demands of efficient conversion of complex organic solid wastes. In recent years, researchers have begun to explore liquid metal catalysis systems with superior thermal conductivity and controllable reactivity, as well as co-pyrolysis approaches involving multi-component organic materials, providing additional perspectives for understanding the dynamic role of metals in pyrolysis processes. For instance, Bharanidharan et al. first reported the catalytic pyrolysis of cellulose using a liquid gallium-tin alloy[25]. They found that the electron-donating characteristics of the liquid metal surface effectively weakened the C-O bond energy in cellulose, facilitating bond cleavage, while the high thermal conductivity of the liquid metal ensured reaction uniformity. More importantly, the free electron cloud at the liquid metal interface coupled with the π orbitals of organic molecules, promoting radical migration and aromatic recombination, thereby achieving higher gas yields and enhanced selectivity toward benzene derivatives. Subsequently, Twizerimana et al. further revealed the dynamic mediating role of liquid metals in ethane dehydrogenation reactions[26]. They demonstrated that liquid metals not only supply reaction heat but also dynamically regulate the reaction pathway through reversible interfacial charge transfer, controlling the energy barriers of reactants and intermediates via electron transport. This finding suggests that liquid metals can be regarded as reaction fields with adaptive electronic structures rather than inert media.

Beyond liquid metal systems, Masnadi and his research team have made systematic contributions in the fields of co-pyrolysis and co-gasification of biomass and fossil fuels [27, 28]. Through kinetic coupling models and experimental validation, they discovered pronounced synergistic and inhibitory effects between metallic and non-metallic components within the system. Metallic elements were found to modulate pyrolysis rates by altering electronic density and the structural order of carbon matrices. These studies reveal that different metallic species in organic pyrolysis systems are not merely passive “catalysts,” but active participants with complex electronic regulation functions. These frontier studies indicate that whether in liquid metal systems or metal-organic composite systems, the mechanistic role of metals in pyrolysis has gradually

shifted from macroscopic catalysis to microscopic electronic regulation. Metallic atoms or ions selectively control pyrolysis pathways and product distributions by tuning molecular orbital energy levels, influencing radical stability, and reshaping the potential energy surface.

Despite these advances, the microscopic electronic regulation role of solid Cu in polymer pyrolysis remains unclear, especially those combining experimental analysis with quantum chemical calculations to elucidate the dynamic regulation of bond energies, radical migration, and product reconstruction by Cu. This study proposes a Cu-assisted dynamic pyrolysis model, we aim to elucidate the electronic structural regulation of Cu and reaction mechanisms using combined experimental and quantum-chemical approaches. This work provides a additional theoretical foundation for the high-value thermochemical conversion of metal-organic composite wastes.

Results

Thermogravimetric and pyrolysis kinetics/thermodynamics analysis

Fig. 1 defines a robust, rate-sensitive stage structure for pyrolysis in the Cu-containing system. Across heating rates of 5~25 °C min^{-1}, the TG/DTG profiles remain highly reproducible and can be consistently partitioned into Stages I-III. Increasing the heating rate shifts both stage boundaries to higher temperature from 222.4 °C at 5 °C min^{-1} to 244.9 °C at 25 °C min^{-1} (StageI→StageII), from 484.7 °C to 512.5 °C (StageII→StageIII), indicating a predictable migration of the apparent rate- controlling regime with thermal history. Mass loss is dominated by Stage II (32.6 ~ 42.3 %), whereas Stage I contributes only 0.5~0.9 %. The DTG maximum likewise shifts to higher temperature and is accompanied by a secondary feature in the 400.7~438.9 °C range, pointing to overlapping contributions from backbone scission and subsequent reorganisation rather than a single-step process. Together, the reproducible staging and systematic peak migration provide a firm basis for discussing a conversion-resolved barrier landscape in following analysis(Figs. 1a-d).

Building on this stage-resolved framework, Fig. 1e converts the macroscopic TG/DTG behaviour into conversion-dependent kinetic and thermodynamic constraints, which speaks

directly to the central message that Cu is not merely an inert residual component, but an intrinsic regulator that reshapes the barrier distribution and reaction pathway as conversion proceeds. The isoconversional analysis reveals a strong increase in the apparent activation energy with α. Using KAS as an example, E_a rises from 137.4 kJ mol^{-1} at α = 0.1 to 206.4 kJ mol^{-1} at α = 0.5, reaching 455.4 kJ mol^{-1} at α = 0.8. Consistently, the six-method accumulated activation energy increases from α = 0.1 to α = 0.8, indicating a transition from rapid mid-stage bond scission to late-stage, high-barrier radical reorganisation/condensation[29, 30]. The thermodynamic reconstruction follows the same trend, ΔH increases from 132.9 to 449.3 kJ mol^{-1}, whereas ΔG increases more modestly, in line with a marked rise and sign change of ΔS at higher conversion-suggesting that although the late-stage process is increasingly enthalpy-demanding, entropic contributions partially offset the free-energy barrier, consistent with a reorganisation/char-forming regime.

Fig. 1e uses $T(\alpha)$ to separate compositional residue effects from genuine pathway shifts. At the same conversion, the Cu-free sample requires systematically higher temperatures to reach the same conversion. For example, α= 0.5: 386.9 °C (Cu-free) vs 365.8 °C (Cu-containing) and α=0.8: 479.0 °C vs 456.3 °C, higher by 21.10 °C and 22.70 °C, respectively. This difference persists even though the absolute final residues differ substantially (Cu-containing about 60% vs Cu-free about 10%), confirming that the Cu effect cannot be reduced to more non-volatile material. Instead, on the more stringent and composition-independent basis of conversion, Cu-containing material reaches the same extent of decomposition at lower temperature, consistent with a modified barrier landscape. Taken together, Fig. 1 establishes a coherent causal chain-three-stage TG/DTG behaviour → conversion- dependent evolution of $E(\alpha)$, ΔH and $\Delta G \rightarrow T(\alpha)$ evidence for Cu-mediated pathway migration-that provides the quantitative foundation for the product distribution and mechanistic analyses that follow. Here, $T(\alpha)$ is used to separate compositional residue effects from genuine pathway shifts, providing a composition-independent basis for comparison. When conducting industrial or semi-industrial pyrolysis experiments of the enameled wire, the effects of stacking configuration and heat transfer within the pyrolysis furnace on both the pyrolysis process and its outcomes should be carefully considered.

Morphological and Elemental Analysis Before and After Pyrolysis

Supplementary Fig. 1 presents the morphology of the raw material and pyrolysis products of polyurethane enameled wire. The raw material has a diameter of approximately 1 mm and is golden yellow in color. The polyurethane enameled wire was cut into 4.5 cm to 6.5 cm lengths for the pyrolysis experiment. The pyrolysis solid products consist of metal copper and pyrolysis carbon. Upon removal from the tubular furnace, the pyrolysis carbon is predominantly attached to the surface of the metal copper, with only a small amount of pyrolysis carbon powder scattered in the crucible. The pyrolyzed enameled wire was removed with tweezers, and a slight shaking effectively separated the metal copper from the pyrolysis carbon. The pyrolysis carbon has a very fine particle size, rich porous structure, excellent adsorption properties, and high stability. The microscopic morphology before pyrolysis as well as the elemental analysis using energy dispersive x-ray spectroscopy are shown in Fig. 2. Before pyrolysis, the surface of the raw material is relatively smooth, with linear indentations or protrusions. When the magnification is increased to 5000×, irregular aggregated protrusions can be observed on the material surface. This is mainly due to the uneven coating of polyurethane enamel on the surface of the metal copper, and the protrusions or indentations on the wire's surface are formed during the manufacturing and molding process. Before pyrolysis, the Cu content is 0%, mainly because the polyurethane encapsulates the metal element Cu. The SEM microstructural analysis reveals the surface morphology of the pyrolysis carbon. The microstructure of the pyrolysis product after pyrolysis is distinctly different from that before pyrolysis(Figs. 2a-e).

The elements detected are C, O, Cu, and N after pyrolysis(97.32%, 0.04%, 1.53%, and 4.12%). After pyrolysis, the content of C increases by 56.21%, the content of O decreases by 47.05%, and the content of N decreases by 7.68%. This is primarily because the pyrolysis process occurs in a N_2 environment(Figs. 2f-j). After the decomposition of polyurethane, the content of pyrolysis carbon increases, and part of the O and N elements are expelled as pyrolysis gases. Analysis of the solid-phase pyrolysis products shows that the Cu content does not substantially increase, indicating that most of the pyrolysis carbon remains covering the surface of the metal Cu. After the pyrolysis

process, the encapsulation behavior of the pyrolysis carbon prevents the metal copper from being easily oxidized, enhancing its recovery and recycling value.

Pyrolysis Experiment and Product Analysis

Fig. 3 provides temperature-resolved marker heatmaps for Cu-containing, Cu-free, and their intensity difference. The Supplementary Fig. 2 shows the flowchart of the pyrolysis experiment. Fig. 3a directly compares Cu-containing and Cu-free pyrolysates and shows that the difference is class- and temperature-dependent rather than a uniform scaling of volatile output. For example, benzene is consistently enriched in the Cu-containing case and reaches 50.4% at 500℃, compared with 44.2% for Cu-free at the same temperature, while oxygenated families are comparatively reduced (phenols at 500 ℃ of 7.9% for Cu-containing and 9.9% for Cu-free). This results support the idea that Cu reshapes pathway competition in the main decomposition region, rather than acting as an inert residue background. Figs. 3b-d and Supplementary Table 1 map how the Cu-containing system distributes products across temperature, linking "pathway selection" to chemically interpretable descriptors. The functional composition shows a structured evolution: benzene rises to a maximum at 500 ℃ (50.4%), whereas CO_2 decreases from 21.3% at 300 ℃ to 13.9% at 500 ℃, indicating that the dominant carbon flux progressively shifts from early gas formation toward aromatic-rich condensables as temperature increases. Importantly, this temperature-resolved profile mirrors the staged behaviour, where the system transitions from rapid scission to a regime where reorganisation and aromatisation become increasingly influential.

The structural statistics reinforce this progression within the Cu-containing products. The light fraction C1~C5 increases from 30.4% (300 ℃) to 42.6% (600 ℃), while the heavier C15~C20 class drops from 24.8% to 8.6%, consistent with a temperature-driven redistribution between fragmentation and secondary transformation. In parallel, the ring-number distribution shifts toward more aromatic architectures, with the two-ring class increasing from 13.4% (300 ℃) to 27.6% (600 ℃). Individual markers peak in distinct temperature windows (with benzene centred around 500 ℃), which is consistent with Cu steering the balance between fragmentation, oxygen removal, and aromatic reorganisation along the heating programme. The two-dimensional FTIR

spectra in Supplementary Fig. 3 reveal pronounced structural transformations of the polyurethane enamel before and after pyrolysis. The pre-pyrolysis sample exhibits characteristic absorptions of urethane functional groups at 3440 cm^{-1} (N-H/O-H stretching), 2930 cm^{-1} (C-H stretching), 1730 cm^{-1} (C=O stretching), 1520 cm^{-1} (amide II band), and 1220-1100 cm^{-1} (C-O and C-N stretching). After pyrolysis, the intensity of these polar absorptions markedly decreases and shifts to lower wavenumbers, indicating preferential cleavage of C-O and C-N bonds. Meanwhile, the aromatic C=C vibration near 1600 cm^{-1} becomes stronger, and two additional bands appear at 805 cm^{-1} and 555 cm^{-1}, corresponding to aromatic ring deformation and weak Cu-O/N coordination vibrations, respectively. These spectral changes are consistent with the DFT-derived electronic structure analysis, suggesting that Cu 3d orbitals form transient coordination with the lone-pair electrons of O and N atoms, thereby modulating local electron density and bond energetics to promote selective cleavage of polar linkages and facilitate aromatic reconstruction during pyrolysis.

Study of the Pyrolysis Mechanism

The bond dissociation energies of different chemical bonds in the polyurethane molecule are shown in Fig. 4. The optimized polyurethane molecular schematic is shown in Supplementary Fig. 4. The bond energy of the C-O bond in the hydroxyl group linked to the benzene ring in the polyurethane molecule is substantially higher than that of the C-O single bond on the other side (450.2>267.9 kJ mol^{-1}). Meanwhile, the C-N bond energies on both sides of the benzene ring in the polyurethane molecule are relatively high, possibly due to conjugation between the nitrogen atom and the carbon atom in the benzene ring(Fig. 4a). However, the bond energy of the C-N bond is notably influenced by the extension groups, with the left C-N bond (linked to the ester group and the benzene ring) having a higher bond energy, while the right C-N bond has a lower bond energy and is more prone to cleavage. The bond energy of the C-O single bond in the ester group is relatively low and easier to break. It can be inferred that during the pyrolysis process, when the energy reaches a certain threshold, the ester C-O bond and the C-N bond on the right side of the benzene ring in the polyurethane molecule break first, generating primary free radicals such as hydroquinone, S1, M1, formic acid, and others(Fig. 4b).

In the second stage of pyrolysis, the chemical bonds in the intermediate pyrolysis products, S1 and M1, randomly break, producing pyrolysis products such as aniline, formaldehyde, benzene, and water. In the third stage of pyrolysis, small molecular free radicals generated in the earlier stages, as well as free radicals from the pyrolysis intermediates, undergo dehydration condensation and re-polymerization to produce a variety of aromatic hydrocarbon compounds, such as terephthalic acid, hydroquinone, biphenyl, methylphenylethylamine, and others. The third stage involves various chemical reactions, including disproportionation, dehydrogenation, dehydration, hydrogenation, and others. Fig. 4c indicate that phenolic aromatic hydrocarbons, under catalytic conditions, can first remove the hydroxyl group and then undergo a dealkylation reaction to form benzene. In the absence of a catalyst, phenolic aromatic hydrocarbons can undergo alkylation to form phenol and then dehydroxylate to form benzene. Two toluene molecules can undergo a disproportionation reaction to generate benzene and para-xylene. Aniline, under certain temperatures and without a catalyst, can also generate benzene. Low molecular weight benzene-ring-containing aromatic hydrocarbons can directly undergo cracking reactions to produce benzene. Toluene and phenol can undergo hydrogenation reactions to generate benzene and small molecular compounds.

The generation patterns and pathways of intermediate product S1 is shown in Fig. 5 and Supplementary Table 2, with energy barrier calculations performed under the condition of 298.15 K. When the pyrolysis pathways are Path1~Path7, the energy barriers of the pyrolysis products are shown in Fig. 5a. In the pyrolysis intermediate product S1, the C-N bond in the non-benzene ring breaks, generating two free radicals, IS2 and IS3, with a bond dissociation energy of 260.9 kJ mol^{-1}. Subsequently, IS2 and IS3 react with hydrogen radicals to generate pyrolysis products S2 and S3. S3 undergoes deamination to form IS5 and IS8, with a bond dissociation energy of 330.9 kJ mol^{-1}. Based on the generation of benzene radicals, the energy barriers for the formation of four characteristic pyrolysis products were calculated: toluene (-133.3 kJ mol^{-1}), aniline (-97.7 kJ mol^{-1}), biphenyl (-148.5 kJ mol^{-1}), benzene (-182.7 kJ mol^{-1}), and ammonia (-155.9 kJ mol^{-1}). There has two additional pyrolysis pathways. The C-N bond on the left side of the benzene ring breaks

first, generating two free radicals, IS4 and IS5, with a bond dissociation energy of 401.2 kJ mol^{-1}(Fig. 5b, Path8~Path14). The C-N chemical bond on the right side of the benzene ring breaks, generating two free radicals, IS6 and IS7, with a bond dissociation energy of 369.6 kJ mol^{-1}. S6 has two decomposition pathways: one involves IS2 and IS5 free radicals, while the other involves IS4 and IS8 free radicals(Fig. 5c, Path15~Path21).

When the pyrolysis pathway is Path22~Path29, the pyrolysis process of M1 is shown in Supplementary Table 3, and the experimental results are depicted in Fig. 5d. The C-O bond on the left side of the benzene ring in the polyurethane molecule first breaks, generating two free radicals, IM2 and IM9, with a bond dissociation energy of 354.1 kJ mol^{-1}. The activation energies for the formation of various pyrolysis products under this reaction pathway were calculated, including benzoic acid (15.8 kJ mol^{-1}), phenol (-51.7 kJ mol^{-1}), biphenyl (-81.0 kJ mol^{-1}), and benzene (-115.1 kJ mol^{-1}). When the C-O bond in the non-benzene ring of M1 initially breaks, leading to a de-aldol reaction that generates free radicals IM3 and IM4, with a bond dissociation energy of 218.4 kJ mol^{-1}. M3, which is phenol, undergoes a dehydroxylation reaction to form both benzene and phenol(Fig. 5e, Path30~Path36). M1 undergoes a dehydroxylation reaction to form IM5 and IM6, with a bond dissociation energy of 403.3 kJ mol^{-1}. The activation energies for the formation of major pyrolysis products such as aniline (55.4 kJ mol^{-1}), o-methyl aniline (21.6 kJ mol^{-1}), and p-phenol (kJ mol^{-1}) were also calculated(Fig. 5f, Path37~Path45). Based on the above research, it can be concluded that in the pyrolysis process of intermediate products S1 and M1, Step 1 involves the cleavage of the C-N bond in the non-benzene ring, which is the most easily broken chemical bond. The corresponding chemical reaction is the de-aldol process, where the activation energy barrier for the formation of free radicals is the lowest. In this case, the aldehyde group released is not conjugated with the benzene ring, and therefore, the chemical bond cleavage occurs more readily. The pyrolysis process of polyurethane molecules generates organic products such as benzene, benzoic acid, aniline, and formic acid, which is consistent with the pyrolysis product distribution results obtained from Py-GC/MS analysis. Furthermore, due to the presence of chemical reactions such as bond cleavage, deamination, de-aldol, dehydroxylation, and free radical

condensation reactions during the pyrolysis process, organic compounds such as biphenyl, p-benzoic acid, and o-methylphenol are generated, which aligns with the experimental results.

Fig. 6 provides a comprehensive comparative analysis of electronic interactions in the EPU system before and after Cu incorporation. Each subpanel corresponds to a different aspect-interaction region (IRI), electrostatic potential (ESP), and orbital energy evolution-but all together delineate how Cu alters the electron distribution and bonding characteristics underlying the catalytic mechanism. The interaction region indicator (IRI) can reveal the distribution of non-bonding interactions in the molecule(Supplementary Fig. 5). If the IRI iso-surface appears reddish, it indicates that there is steric hindrance between the chemical bonds. If the IRI iso-surface is green, it suggests that the dominant interaction in this region is van der Waals forces or possibly weak hydrogen bonding. The computational analysis reveals that, in the absence of copper atoms, various types of chemical bonds exist at different positions within the polyurethane molecule. Covalent bonds are observed throughout the molecular backbone, alongside hydrogen bonds and steric hindrance effects within the benzene rings(ρ>0), typically located between atoms such as C-C, C-N, and C-H. The presence of hydrogen bonds reinforces intermolecular cohesion and stabilizes the overall molecular conformation(Figs. 6a-d). However, The incorporation of copper substantially alters both the intra- and intermolecular interaction networks, thereby affecting the stability and chemical properties of polyurethane(Fig. 6e). Copper atoms modify the overall electronic distribution, concentrating the covalent bonding regions and reinforcing the rigidity of the molecular skeleton. Moreover, copper forms coordination bonds with oxygen and nitrogen atoms within the molecule, indicative of its coordination chemistry. Regions surrounding the copper atom exhibit increased and uneven electron density, which can substantially impact molecular reactivity. The IRI vs. sign $(\lambda_2)\rho$ scatter plot for the polyurethane system is presented. Two distinct clusters are observed, the left cluster corresponds to weaker van der Waals and hydrogen bonding interactions, while the right cluster represents stronger covalent bonds. Upon copper incorporation, the distribution becomes broader, indicating a redistribution of electrons and enhancement of covalent bonding, hydrogen bonding, and steric effects. Additionally, the peak of

the overall density distribution shifts slightly toward the attractive interaction region, suggesting that copper enhances weak attractive interactions both within and between molecules(Fig. 6f).

The relationship between ESP and molecular surface area with and without copper are summarized. Areas of negative ESP dominate and are primarily located around oxygen atoms, particularly near carbonyl groups and other highly electronegative sites(Supplementary Tables 4, 5). In the absence of copper, the electrostatic potential distribution is largely determined by polar functional groups such as carbonyl and amino groups, and displays a relatively uniform distribution characteristic of typical organic molecules. In contrast, compared to the copper-free system, both the positive and negative extremes of ESP are increased. While negative ESP remains concentrated around oxygen atoms, the introduction of positively charged copper ions leads to partial attenuation or redistribution of these regions. Meanwhile, regions of positive ESP become substantially more pronounced, particularly around the Cu center, consistent with an enhanced local electrostatic field associated with Cu (Supplementary Figs. 6, 7). Such a shift facilitates stronger interactions with negatively charged species, potentially enhancing the molecule's thermal decomposition activity. The introduction of copper strengthens electrostatic interactions within and around the molecule, leading to greater charge separation and polarization effects.

In the copper-containing system, both HOMO and LUMO energy levels are substantially increased, reaching -0.13447 a.u. and -0.04352 a.u., respectively, with a substantially smaller energy gap(Fig. 6g). The increase in HOMO indicates that the introduction of copper alters the electronic distribution of the system, weakening the electron-donating ability. The increase in LUMO reflects that the high positive charge of copper reduces the electron-capturing ability, resulting in an upward shift of the lowest unoccupied molecular orbital. The smaller energy gap suggests that copper's introduction reduces the energy required for electron transitions between molecules, substantially promoting the thermal decomposition process of polyurethane. In the copper-free system, the HOMO and LUMO distributions are more diffuse, indicating a broader range of overall charge transfer across the molecule. LUMO and HOMO are distributed in Cu and its surrounding O/N regions, indicating that Cu 3d orbitals are involved in frontier orbital coupling.

The introduction of copper notably changes the frontier orbital distribution and energy level structure of the polyurethane molecule. Furthermore, the more localized distributions of HOMO and LUMO enhance the system's ability for localized charge transfer. The introduction of copper substantially facilitates the thermal decomposition of the polyurethane-coated wire.

The electrostatic potential ranges for M1 are -31.0 kcal mol^{-1} to 54.0 kcal mol^{-1}. Compared with M1, the electrostatic potential distribution of S1 is more extensive, with a marked increase in the blue region, indicating a lower overall electron density and stronger electron-accepting ability. Fig. 7 shows that the electrostatic potential distribution of M1 is uniform, with nearly equal distribution of positive and negative charges. However, for S1, the negative charge region substantially increases, indicating that S1 is more electrophilic. The HOMO and LUMO energy levels of M1 and S1 are -0.22905 a.u. and -0.02551 a.u., and -0.19790 a.u. and -0.01157 a.u., respectively. The lower HOMO-LUMO energy gap for S1 indicates that it is more reactive and more prone to electronic transitions than M1(Figs. 7a, b). The introduction of copper substantially alters the electrostatic potential distribution of M1, with a noticeable increase in the positive region. It's obviously that the HOMO-LUMO energy gap is substantially reduced. After the introduction of copper, the overall electrostatic potential range of S1 increases, but its nucleophilicity is slightly lower than that of M1. The copper atom participates in the formation of molecular orbitals, and the effect of copper on S1 is slightly weaker than on M1(Supplementary Tables 6-9).

After copper is introduced, the positive electrostatic potential region of M1 increases, showing that Cu enhances the nucleophilicity. For S1+Cu, the positive region is smaller than that in M1+Cu, but still substantially larger than in the copper-free M1 and S1 systems. The introduction of copper reduces the HOMO- LUMO energy gap of the main thermal decomposition intermediates S1 and M1, increasing the chemical reactivity(Figs. 7c, d). The electrostatic potential distribution shows an increase in the positive region, indicating that metallic Cu has a strong regulatory effect on the electronic properties of the system. Compared to M1, S1's electrostatic potential tends toward negative values, indicating higher chemical reactivity. The reactivity regulation of the typical thermal decomposition intermediate S1 by metallic Cu is slightly weaker

than that of M1(Figs. 7e-h). The results above proposes a Cu-assisted dynamic pyrolysis model, in which copper acts as an electronic regulatory center rather than a passive thermal medium. The model identifies three synergistic mechanisms. First, Cu 3d orbitals transiently coordinate with O/N atoms, concentrating electron density and narrowing the HOMO-LUMO gap. Second, this coordination stabilizes radicals and suppresses side reactions. Third, reversible Cu^0/Cu^+ cycling promotes electron migration and aromatic reconstruction.These findings provide a quantum-level understanding of Cu as a dynamic electronic regulator in thermochemical decomposition.

Discussion

This work clarifies that metallic Cu in polyurethane enamel pyrolysis is not an inert heat-transfer/residual background, but an active participant that reshapes the conversion-dependent barrier landscape and thereby redirects reaction pathways. By integrating thermogravimetric/isoconversional kinetics with temperature-resolved product fingerprints, we show that Cu effects are expressed as pathway selectivity rather than a simple scaling of volatilisation. The observed staged decomposition and the evolution of apparent barriers with conversion support a late-stage regime dominated by radical reorganisation, condensation and char-forming transformations, providing a quantitative basis to interpret how Cu changes the conditions required to reach the same extent of conversion.

Density functional theory offers a mechanistic origin for this behaviour. Cu forms reversible Cu-O/N coordination with oxygen and nitrogen sites in polyurethane, which narrows the HOMO-LUMO gap and strengthens electron transfer and radical recombination propensity. As a result, the competition between key bond-cleavage and rebuilding channels is shifted, favouring selective scission of C-O and C-N linkages and facilitating downstream aromatisation. This electronic regulation mechanism rationalises why the Cu-containing system exhibits structured, temperature-dependent product redistribution rather than indiscriminate cracking.

Based on these combined results, we propose a dynamic Cu-assisted decomposition framework in which Cu operates through a coupled sequence of (i) electronic-structure regulation

via reversible coordination, (ii) transient stabilisation of reactive intermediates that suppresses unselective condensation, and (iii) redox-enabled cycling that promotes reorganisation toward aromatic structures at advanced conversion. While the heating programmes studied here are milder than those in industrial reactors, the mechanistic picture and the conversion-resolved descriptors established in this work provide a transferable foundation for testing high-rate and reactor-scale conditions. More broadly, our findings advance a general paradigm for thermochemical valorisation of metal-organic composite wastes, where endogenous metals can act as electronic regulators that couple molecular-scale chemistry to macroscopic process behaviour.

Methods

Sample preparation and pyrolysis experiments

The polyurethane enameled wire used in this study was sourced from a materials company based in Zhejiang Province, China. The wire has a diameter of approximately 1.2 mm and consists of a copper core coated with a layer of polyurethane enamel. For experimental purposes, the enameled wire was cut into 1.5 cm segments for thermogravimetric analysis and 5 cm segments for pyrolysis experiments. During the experiments, a nitrogen flow rate of approximately 70 mL/min was maintained to ensure an oxygen-free atmosphere.

Thermogravimetric Analysis and Pyrolysis Kinetics

Thermogravimetric analysis (TGA) was conducted on a HITACHI 6300 thermal analyser to probe the oxygen-free thermal decomposition of polyurethane enameled copper wire under high-purity nitrogen[31-33]. The nitrogen flow was maintained at 70 mL/min throughout the experiment. Samples were cut into short segments and weighed to 5.5 ± 0.1 mg for each run. the temperature was ramped from ambient to 950 ℃ at heating rates of 5, 10, 15 and 25 ℃ min^{-1}. Each condition was measured in triplicate to ensure reproducibility, and the averaged curves were used for subsequent analysis. The mass-conversion degree (α) was calculated from the TG curves. To ensure robust isoconversional fitting, kinetic calculations were performed over 0.1~0.8.

Conversion-dependent kinetic parameters were derived using model-free isoconversional analyses. Six methods kinetic methods, Flynn-Wall-Ozawa (FWO), Kissinger-Akahira-sunose(KAS), Friedman, Starink, Tang, and Vyazovkin, were applied. In all regressions and calculations, temperature was expressed in Kelvin. The resulting were used to quantify barrier evolution across the staged decomposition process and to support subsequent thermodynamic analysis[34-38].

SEM-EDS

The microstructural morphology of the raw material and solid-phase products was analyzed using scanning electron microscopy (SEM, Zeiss Gemini300). SEM images before and after pyrolysis were captured at magnifications corresponding to scale bars of 2 μm and 10 μm, respectively, with resolutions of 10000 and 50000. Elemental mapping of the solid-phase materials before and after pyrolysis was conducted using energy-dispersive X-ray spectroscopy (EDS, Oxford Ultim Extreme). The atomic percentages of four key elements (C, O, N, Cu) were quantitatively analyzed to evaluate compositional changes during pyrolysis. Elemental quantification in SEM-EDS surface scans was controlled within an error range of ±1.5%. The main data all remain within a reasonable range.

Py-GC/MS

Pyrolysis-gas chromatography/mass spectrometry (Py-GC/MS) analysis was performed using a GCMS-QP2010 Ultra system, equipped with an EGA/PY-3030D pyrolyzer. The thermal degradation products of polyurethane enameled wire with and without copper were analyzed at pyrolysis temperatures of 300 °C, 400 °C, 450 °C, 500 °C, 550 °C, and 600 °C. Each experiment was repeated twice for reproducibility. Py-GC/MS quantification was performed using the relative peak area method, based on past experience it can be known that due to incomplete resolution of some high-boiling-point compounds, the measured concentrations of benzene and its derivatives may carry a systematic error of approximately ±3%. The main data all remain within a reasonable range. The pyrolysis was carried out under a high-purity N_2 atmosphere to ensure an oxygen-free environment. Under such conditions, oxidation of Cu is

thermodynamically prohibited, and the Cu valence evolution primarily involves reduction and electronic redistribution.

FT-IR

The pre-pyrolysis samples were gently flattened to ensure full contact between the coating surface and the ATR crystal, while the post-pyrolysis solid residues were finely ground to improve surface contact during ATR measurement. Fourier-transform infrared (FTIR) spectra were recorded using a Bruker Vertex 70 spectrometer equipped with an attenuated total reflectance (ATR) accessory fitted with a ZnSe crystal. The wavenumber range was 4000-400 cm^{-1}. The post-pyrolysis solid residues were finely ground prior to measurement.

Quantum chemistry calculations

The bond dissociation energies of various chemical bonds in the polyurethane molecule were calculated using the Gaussian 09, with molecular models constructed in Gaussian View 6.0[39-41]. Molecular geometry optimizations for pyrolysis-related organic compounds, intermediates, and products were performed based on the same functional and basis set, namely M06-2X/6-311G. The BDEs of the involved chemical bonds were calculated using enthalpy free energy, while the energy barriers of pyrolysis reactions were determined using Gibbs free energy. All molecular optimizations were conducted under standard conditions (298.15 K and 1 atm), with enthalpy and Gibbs free energies corrected using Shermo 2.3.4 (scaling factor: 0.970). An estimated single-point energy uncertainty of ±0.05 eV. In addition, the frontier molecular orbitals and electrostatic potential distributions of the polyurethane molecule and typical pyrolysis products were analyzed under both Cu-present and Cu-absent conditions using computational visualization tools including Gaussian 09, VMD version 1.94, and Multiwfn 3.8[42].

Data availability

All supplementary data supporting the findings of this study are available in zenodo at doi: https://zenodo.org/records/18414263(ref. 43).

References

1. Yang C*, et al.* Copper-coordinated cellulose ion conductors for solid-state batteries. *Nature* **598**, 590-596 (2021).
2. Vavra J*, et al.* Solution-based Cu+ transient species mediate the reconstruction of copper electrocatalysts for CO2 reduction. *Nature Catalysis* **7**, 89-97 (2024).
3. Born K, Ciftci MM. The limitations of end-of-life copper recycling and its implications for the circular economy of metals. *Resources, Conservation and Recycling* **200**, 107318 (2024).
4. Mudd GM, Jowitt SM. Growing global copper resources, reserves and production: Discovery is not the only control on supply. *Economic Geology* **113**, 1235-1267 (2018).
5. Sovacool BK*, et al.* Sustainable minerals and metals for a low-carbon future. *Science* **367**, 30-33 (2020).
6. Luo X, Pan L, Yang J. Mineral resource constraints for China's clean energy development under carbon peaking and carbon neutrality targets: quantitative evaluation and scenario analysis. *Energies* **15**, 7029 (2022).
7. Shittu OS, Williams ID, Shaw PJ. Global E-waste management: Can WEEE make a difference? A review of e-waste trends, legislation, contemporary issues and future challenges. *Waste Management* **120**, 549-563 (2021).
8. Rene ER*, et al.* Electronic waste generation, recycling and resource recovery: Technological perspectives and trends. *Journal of hazardous materials* **416**, 125664 (2021).
9. Gu Y, Wu Y, Xu M, Mu X, Zuo T. Waste electrical and electronic equipment (WEEE) recycling for a sustainable resource supply in the electronics industry in China. *Journal of Cleaner Production* **127**, 331-338 (2016).
10. Widijatmoko SD, Cui ZJ, Agalit H, Li Y, Leeke GA. Recycling of enamelled copper wire from end-of-life electric motor via room temperature methanolysis. *Resources, Environment and Sustainability* **15**, 100143 (2024).
11. Hagedorn J, Blanc FS-L, Fleischer J. Enamelled copper wire. In: *Handbook of Coil Winding: Technologies for efficient electrical wound products and their automated production*). Springer (2018).
12. Mastoi MS*, et al.* A comprehensive analysis of the power demand–supply situation, electricity usage patterns, and the recent development of renewable energy in China. *Sustainability* **14**, 3391 (2022).
13. Bhanu VA. Polyester Wire Enamels-Reliable Coatings in the Wire Industry from the Beginning to Nowadays. *Macromolecular Materials and Engineering* **293**, 340-349 (2008).
14. Li X, Ma B, Wang C, Chen Y. Sustainable recovery and recycling of scrap copper and alloy resources: A review. *Sustainable Materials and Technologies*, e01026 (2024).
15. Zhang W*, et al.* Analyzing the environmental impact of copper-based mixed waste recycling-a LCA case study in China. *Journal of Cleaner Production* **284**, 125256 (2021).
16. Zhang L, Xu Z. A review of current progress of recycling technologies for metals from waste electrical and electronic equipment. *Journal of Cleaner Production* **127**, 19-36 (2016).

17. Ma S, Xing P, Li H, Wang C, Liu M, Xu B. Efficient and emission-reduced recovery of high-purity copper from waste enameled copper wires. *Resources, Conservation and Recycling* **212**, 107903 (2025).
18. Choukri O, Mohsine E, Taibi S. Industrial Recycling of Scrap Copper Cables and Wires: Combining Cold and Hot Treatments for Maximum Recovery and Minimal Emissions. *Archives of Foundry Engineering*, (2024).
19. Wang X*, et al.* Effects of copper (II) oxide on the co-pyrolysis of waste polyester enameled wires and poly (vinyl chloride). *Polymers* **16**, 27 (2023).
20. Tao R*, et al.* Co-pyrolysis mechanism of polyester enameled wire and PVC: A joint experimental and theoretical investigation. *Journal of Cleaner Production* **446**, 141358 (2024).
21. Cui J, Forssberg E. Mechanical recycling of waste electric and electronic equipment: a review. *Journal of hazardous materials* **99**, 243-263 (2003).
22. Barbakadze K, Brostow W, Granowski G, Hnatchuk N, Lohse S, Osmanson AT. Separation of metal and plastic wastes from wire and cable manufacturing for effective recycling. *Resources, Conservation and Recycling* **139**, 251-258 (2018).
23. Begum YA, Kumari S, Jain SK, Garg MC. A review on waste biomass-to-energy: integrated thermochemical and biochemical conversion for resource recovery. *Environmental Science: Advances*, (2024).
24. Elgarahy AM*, et al.* Revitalizing the circular economy: an exploration of e-waste recycling approaches in a technological epoch. *Sustainable Chemistry for the Environment*, 100124 (2024).
25. Bharanidharan, A.H., McGaughy, K., Twizerimana, A.L., Ocampo, K., Veser, G., & Masnadi, M.S. Cellulose pyrolysis via liquid metal catalysis. *Journal of Analytical and Applied Pyrolysis* **183**, 106800 (2024).
26. Twizerimana, A.L., Bharanidharan, A.H., McGaughy, K., Ocampo, K., Parker, C.E., Masnadi, M.S., & Veser, G. Liquid metals as robust reaction media for ethane dehydrogenation. *Energy & Fuels* **39**, 8239-8247. (2025).
27. Masnadi, M.S., Habibi, R., Kopyscinski, J., Hill, J.M., Bi, X., Lim, C.J., Ellis, N., & Grace, J.R. Fuel characterization and co-pyrolysis kinetics of biomass and fossil fuels. *Fuel* **117** , 1204-1214. (2014).
28. Masnadi, M.S., Grace, J.R., Bi, X.T., Lim, C.J., & Ellis, N. From fossil fuels towards renewables: Inhibitory and catalytic effects on carbon thermochemical conversion during co-gasification of biomass with fossil fuels. *Applied Energy* **140**, 196-209. (2015).
29. Ikpeseni SC*, et al.* Pyrolysis characteristics and kinetics of the thermal degradation of elephant grass (Pennisetum purpureum): a comparative analysis using the Flynn–Wall–Ozawa and the Kissinger–Akahira–Sunose methods. *Environment, Development and Sustainability*, 1-19 (2023).
30. Aniza N, Hassan S, Nor M, Fadhil M. Kinetic Analysis of Poultry Processing Dewatered Sludge (PPDS) Using Thermogravimetric Analysis (TGA). In: *MATEC Web of Conferences*). EDP Sciences (2014).
31. Xianfeng Y*, et al.* Study of thermal degradation mechanism of binders for ceramic injection molding by TGA-FTIR. *Ceramics International* **45**, 10707-10717 (2019).

32. Chetehouna K, Belayachi N, Rengel B, Hoxha D, Gillard P. Investigation on the thermal degradation and kinetic parameters of innovative insulation materials using TGA-MS. *Applied Thermal Engineering* **81**, 177-184 (2015).
33. Cervantes-Uc J, Cauich-Rodríguez J, Vázquez-Torres H, Licea-Claveríe A. TGA/FTIR study on thermal degradation of polymethacrylates containing carboxylic groups. *Polymer degradation and stability* **91**, 3312-3321 (2006).
34. Foltin JP, Prado GN, Lisbôa AC. Analysis of kinetics parameters of oil shale pyrolysis. *CHEMICAL ENGINEERING* **61**, (2017).
35. Wang L, Li Yh, Lu Jl, Xu W, Lin Hl. Thermal decomposition kinetics of manganese carbonate in the process of mnzn ferrite preparation. In: *TMS 2016: 145th Annual Meeting & Exhibition: Supplemental Proceedings: Supplemental Proceedings*). Wiley Online Library (2016).
36. Li H, Niu S, Lu C. Thermal characteristics and kinetic calculation of castor oil pyrolysis. *Procedia Engineering* **205**, 3711-3716 (2017).
37. Handawy MK, Snegirev AY, Stepanov V, Talalov V. Kinetic modeling and analysis of pyrolysis of polymethyl methacrylate using isoconversional methods. In: *IOP Conference Series: Materials Science and Engineering*). IOP Publishing (2021).
38. Shawabkeh A, Abdel Halim K, Al-Ayed O. Isoconversional methods for kinetic modeling of kerogen pyrolysis using TG data. *Applied Mechanics and Materials* **835**, 299-307 (2016).
39. Pang Z, Huang S, Li Y, Zhang Y, Qin R. Molecular Simulation Analysis of Polyurethane Molecular Structure under External Electric Field. *Molecules* **29**, 4329 (2024).
40. Saha JK, Rahman MM, Haq MB, Al Shehri DA, Jang J. Theoretical and experimental studies of hydrogen bonded dihydroxybenzene isomers polyurethane adhesive material. *Polymers* **14**, 1701 (2022).
41. Zhang C, Hu J, Chen S, Ji F. Theoretical study of hydrogen bonding interactions on MDI-based polyurethane. *Journal of molecular modeling* **16**, 1391-1399 (2010).
42. Lu T, Chen F. Multiwfn: A multifunctional wavefunction analyzer. *Journal of computational chemistry* **33**, 580-592 (2012)
43. Zhang,W. Reversible copper coordination redirects pyrolysis products in waste polyurethane enamelled copper wire. Zenodo https://zenodo.org/records/18414263 (2026).

Fig. 1 | Thermogravimetric behaviour and conversion-dependent kinetics of Cu-containing and Cu-free samples. a-d TG/DTG curves recorded under N_2 at 5, 10, 15 and 25 °C min^{-1}, showing a consistent three-stage decomposition (stage boundaries marked from DTG features). **e** Conversion-resolved analyses based on multi-rate TG data, including six isoconversional methods (Vyazovkin, Tang, Starink, Friedman, KAS and FWO), TG/DTG comparison of Cu-containing and Cu-free samples, $T(\alpha)$-α, and $\Delta H/\Delta G/\Delta S$-$\alpha$. TG is plotted on a whole-sample basis (polymer+Cu); therefore, comparisons rely on α and $T(\alpha)$ rather than absolute residue levels.

Fig. 2 | SEM and EDS images before and after pyrolysis. Before pyrolysis: **a** SEM images. **b** Layered image. **c** Spectrum. **d** Elemental composition and content. **e** Elemental spectrum of C/O/Cu/N. After pyrolysis: **f** SEM images of EPU. **g** Layered image. **h** Spectrum. **i** Elemental composition and content. **j** Elemental spectrum of C/O/Cu/N.

Fig. 3 | Relative content variation of pyrolysis products under different temperatures (300°C/400°C/450°C/500°C/550°C/600°C). a Temperature-resolved marker heatmaps for Cu-containing, Cu-free, and their intensity difference. **b** Temperature-dependent functional-group distribution of pyrolysis products. **c** Carbon-number and aromatic ring-number distributions of pyrolysis products at different temperatures. **d** Temperature-dependent yields of representative marker compounds (selected chlorinated/aromatic/oxygenated/CO_2 markers).

Fig. 4 | Pyrolysis mechanism of polyurethane organic coatings based on density functional theory and quantum chemistry calculations. a EPU model compounds and bond dissociation energy (kJ mol^{-1}) based on M062X/6-311(d,p). **b** Detailed three-stage pyrolysis process of EPU and potential pyrolysis pathways. **c** Formation process of benzene.

Fig. 5 | Reaction pathway energy barriers for typical pyrolysis products. a, **b**, **c** Energy barriers for different reaction pathways of typical pyrolysis product S1. **d**, **e**, **f** M1.

Fig. 6 | Comparative analysis of electronic structure and interactions. Without copper: **a** Interaction region inside polyurethane molecular. **b** IRI vs sign$(\lambda_2)\rho$ scatter plot. **c** LUMO and HOMO energy levels. **d** Van der Waals(VdW) surface ESP map. With copper: **e** Interaction region between EPU and Cu. **f** IRI vs sign$(\lambda_2)\rho$ scatter plot. **g** LUMO and HOMO energy levels α orbitals and β orbitals.

Fig. 7 | ESP maps and frontier molecular orbital diagrams of typical pyrolysis intermediates. The VdW surface ESP map and LUMO and HOMO energy levels of **a** M1, **b** S1, **c** M1 with copper, **d** S1 with copper. Histogram distributions of ESP areas of **e** M1, **f** S1, **g** M1 with copper, **h** S1 with copper.

Acknowledgement

This work was financially supported by the National Key Research and Development Program of China(2022YFC3902604), National Science Foundation for Distinguished Young Scholars of China (52425004), National Natural Science Foundation of China Original Exploration Program(52554013), Science and Technology General Project of Beijing Municipal Education Commission(KM202410005001).

Author contributions

W.Z. and X.Z. completed the thermogravimetric experiment, composition distribution of pyrolysis products, data collection and data analysis. W.Z. completed the SEM-EDS analysis and picture data collection. Y.G completed the calculation of bond energy of chemical bond in polyurethane molecule. W.Z. and L.Z completed the Infrared spectral analysis and electrostatic potential distribution on molecular surface. R.T and B.L. helped analyze the results of quantum chemistry calculations. All authors were involved. W.Z. wrote the manuscript, and all the authors revised the paper. Y.W. supervised the project.

Competing interests

The authors declare no competing interests.

Additional information

Supplementary information The online version contains supplementary material.

Correspondence and requests for materials should be addressed to Yufeng Wu.

Editorial summary:

Copper significantly redirects the pyrolysis of waste polyurethane-enamelled copper wire through electronic-structure regulation, reversible copper oxygen/nitrogen coordination, and frontier-orbital coupling, according to a copper-assisted dynamic pyrolysis model.

Peer review information:

Communications Earth and Environment thanks Samuel Widijatmoko and the other, anonymous, reviewer(s)

for their contribution to the peer review of this work. Primary Handling Editor: Nandita Basu. [A peer review file is available.]

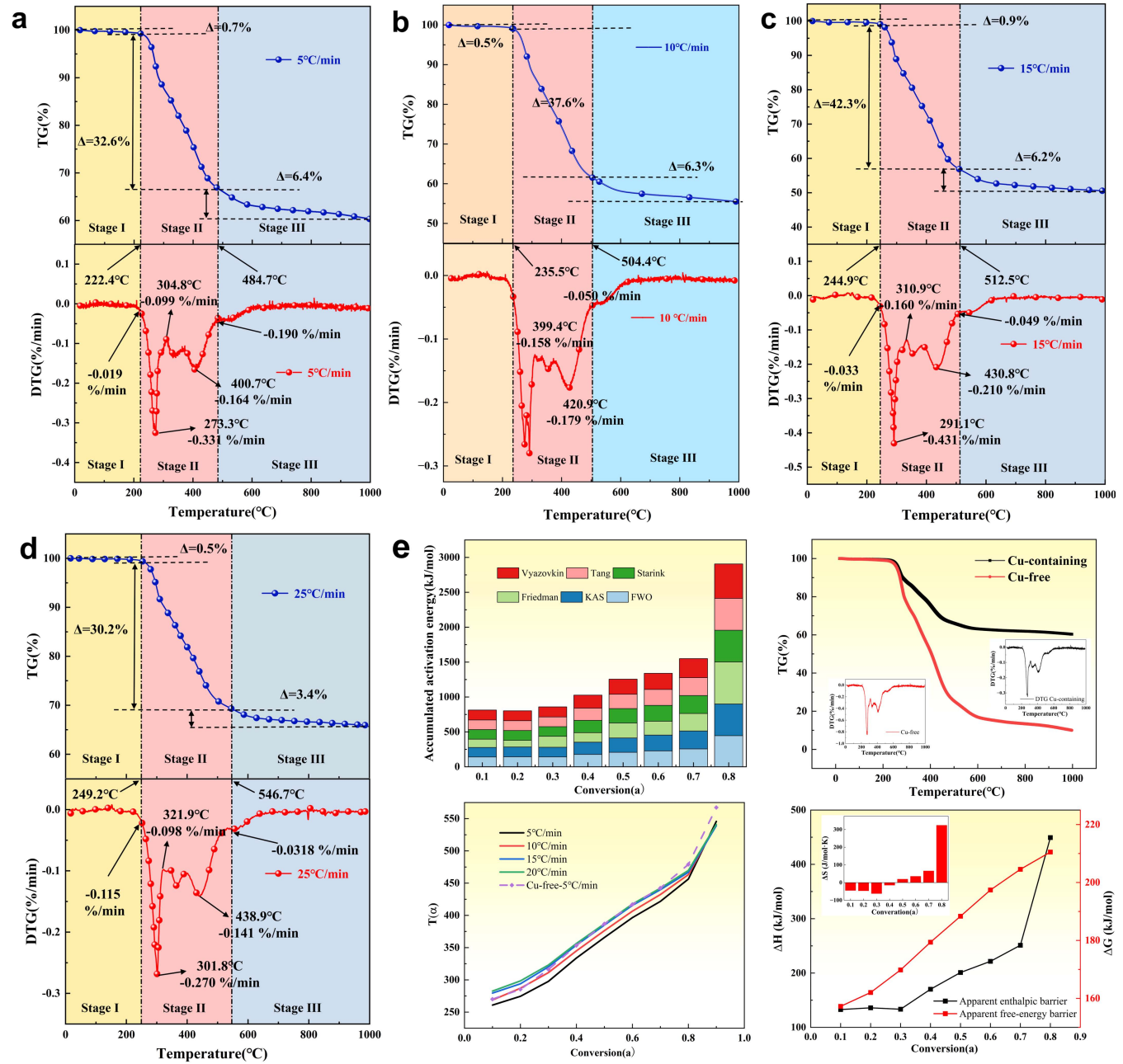
a
TG(%)
Δ=0.7%
5°C/min
Δ=32.6%
Δ=6.4%
Stage I
Stage II
Stage III
DTG(%/min)
222.4°C
304.8°C
-0.099 %/min
484.7°C
-0.190 %/min
-0.019 %/min
5°C/min
400.7°C
-0.164 %/min
273.3°C
-0.331 %/min
Temperature(°C)
b
TG(%)
Δ=0.5%
10°C/min
Δ=37.6%
Δ=6.3%
DTG(%/min)
235.5°C
504.4°C
-0.050 %/min
10 °C/min
399.4°C
-0.158 %/min
420.9°C
-0.179 %/min
Temperature(°C)
c
TG(%)
Δ=0.9%
15°C/min
Δ=42.3%
Δ=6.2%
DTG(%/min)
244.9°C
310.9°C
-0.160 %/min
512.5°C
-0.049 %/min
15°C/min
-0.033 %/min
430.8°C
-0.210 %/min
291.1°C
-0.431 %/min
Temperature(°C)
d
TG(%)
Δ=0.5%
25°C/min
Δ=30.2%
Δ=3.4%
DTG(%/min)
249.2°C
321.9°C
-0.098 %/min
546.7°C
-0.0318 %/min
25°C/min
-0.115 %/min
438.9°C
-0.141 %/min
301.8°C
-0.270 %/min
Temperature(°C)
e
Accumulated activation energy(kJ/mol)
Vyazovkin
Tang
Starink
Friedman
KAS
FWO
Conversion(a)
T(α)
5°C/min
10°C/min
15°C/min
20°C/min
Cu-free-5°C/min
Conversion(a)
TG(%)
Cu-containing
Cu-free
DTG Cu-containing
Cu-free
Temperature(°C)
ΔH (kJ/mol)
ΔS (J/mol·K)
Conversion(a)
Apparent enthalpic barrier
Apparent free-energy barrier
ΔG (kJ/mol)
Conversion(a)

Before pyrolysis

a

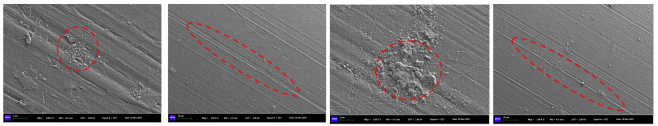

b

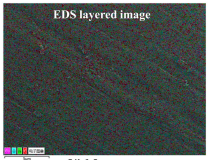

c

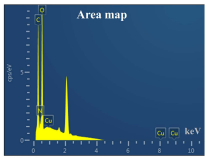

d

Area map

element	line style	weight percentage	wt% Sigma	atomic percent
C	K	34.96	0.29	41.11
O	K	53.34	0.36	47.09
Cu	L	0.00	0.21	0.00
N	K	11.70	0.48	11.8
Total		100.00		100.0

e

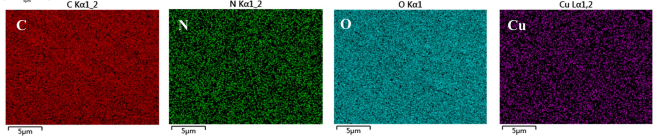

After pyrolysis

f

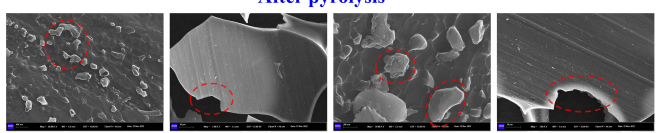

g

h

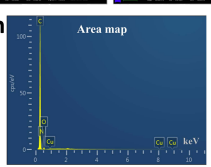

i

Area map

element	line style	weight percentage	wt% Sigma	atomic percent
C	K	92.66	0.35	94.32
O	K	0.21	0.04	0.04
Cu	L	1.75	0.36	1.53
N	K	5.39	0.09	4.12
Total		100.00		100.0

j

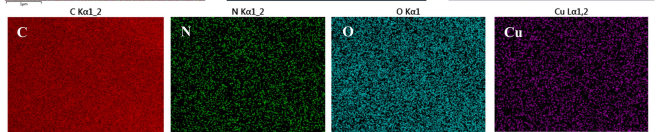

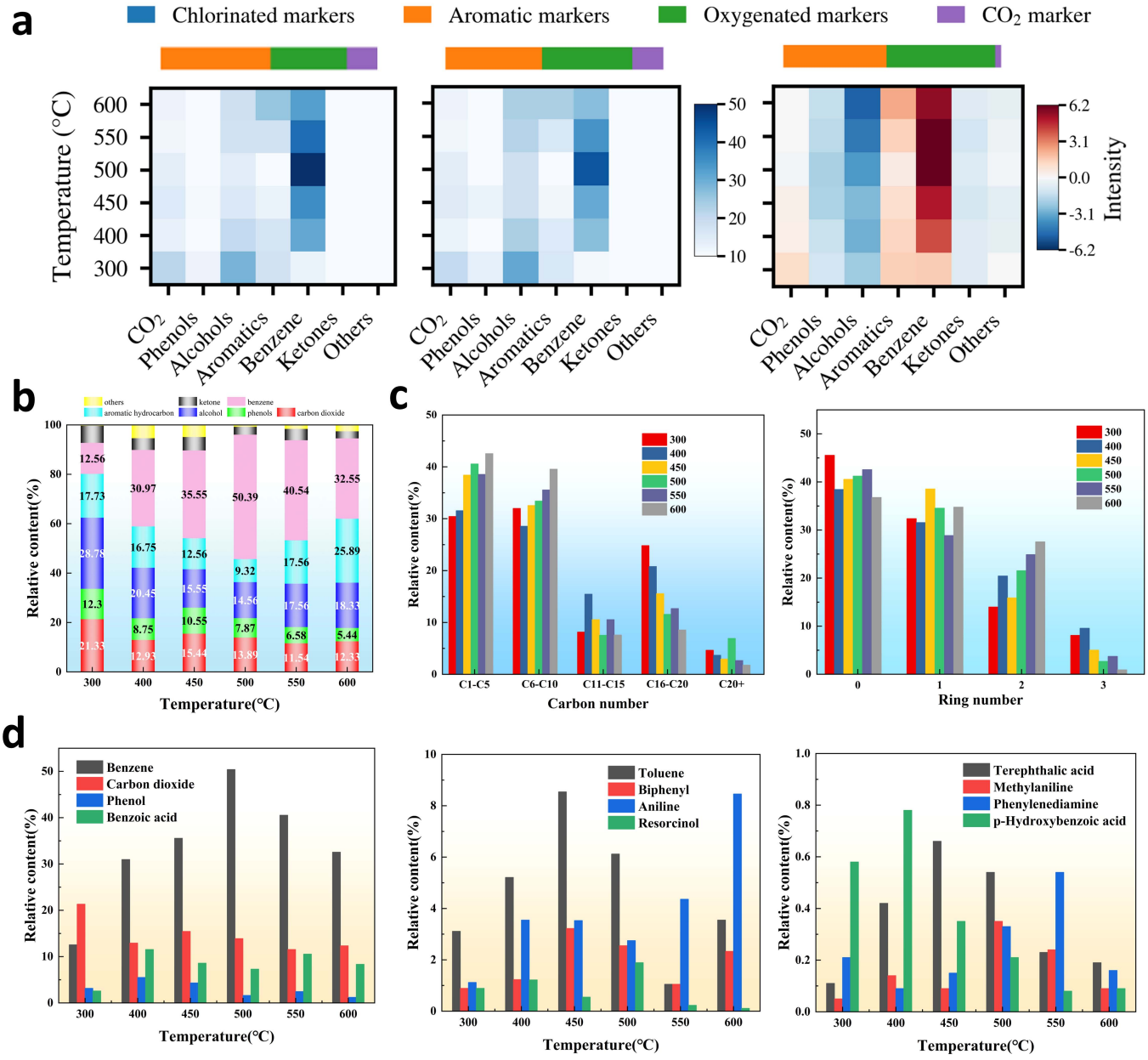
a
Chlorinated markers
Aromatic markers
Oxygenated markers
CO2 marker
Temperature (°C)
600
550
500
450
400
300
CO2
Phenols
Alcohols
Aromatics
Benzene
Ketones
Others
50
40
30
20
10
6.2
3.1
0.0
-3.1
-6.2
Intensity
b
others
aromatic hydrocarbon
ketone
alcohol
benzene
phenols
carbon dioxide
Relative content(%)
Temperature(°C)
c
Relative content(%)
C1-C5
C6-C10
C11-C15
C16-C20
C20+
Carbon number
Ring number
d
Benzene
Carbon dioxide
Phenol
Benzoic acid
Toluene
Biphenyl
Aniline
Resorcinol
Terephthalic acid
Methylaniline
Phenylenediamine
p-Hydroxybenzoic acid

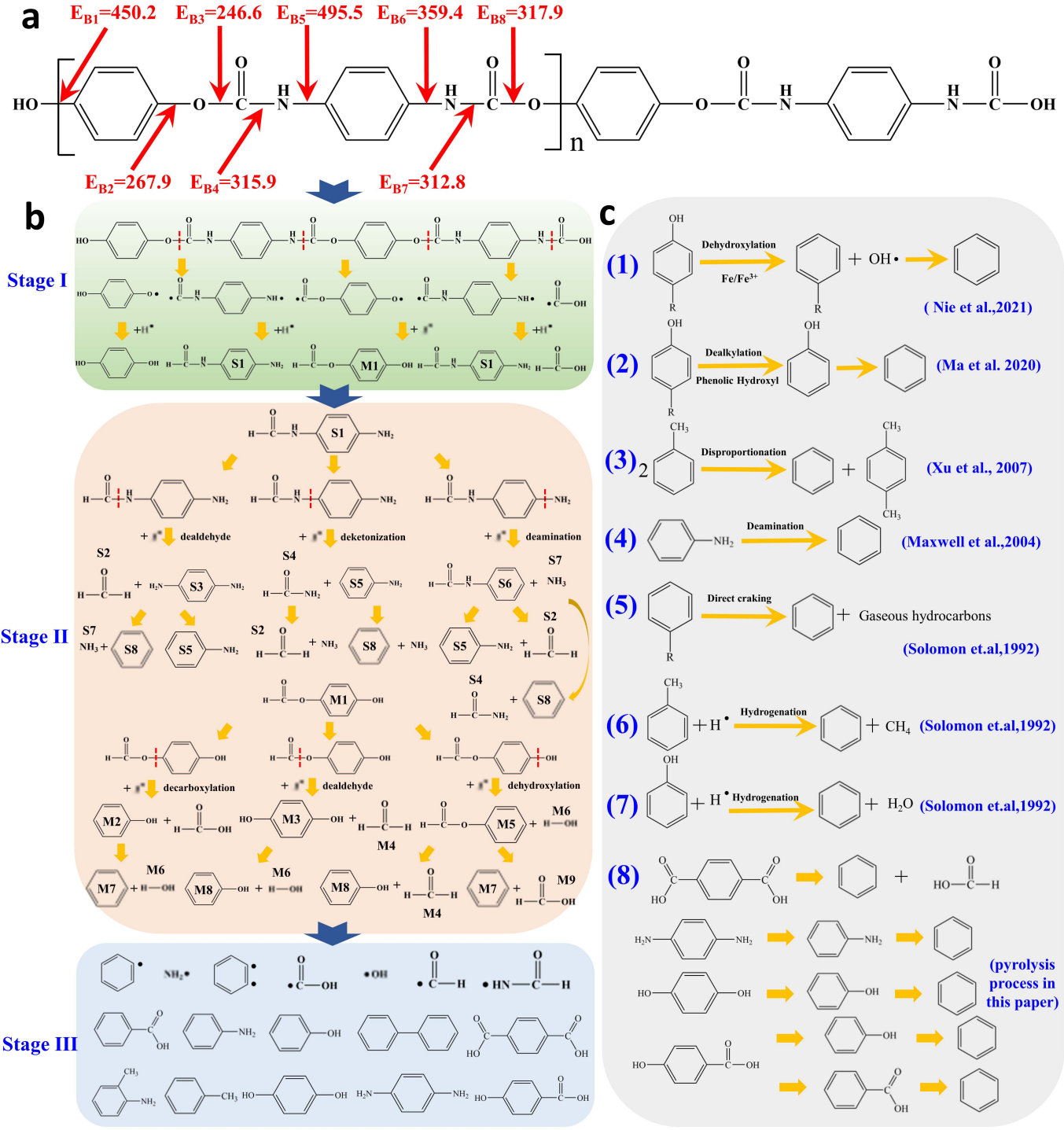
a
E_{B1}=450.2
E_{B3}=246.6
E_{B5}=495.5
E_{B6}=359.4
E_{B8}=317.9
E_{B2}=267.9
E_{B4}=315.9
E_{B7}=312.8
b
Stage I
Stage II
Stage III
dealdehyde
deketonization
deamination
decarboxylation
dealdehyde
dehydroxylation
c
(1)
Dehydroxylation
Fe/Fe3+
(Nie et al.,2021)
(2)
Dealkylation
Phenolic Hydroxyl
(Ma et al. 2020)
(3)
Disproportionation
(Xu et al., 2007)
(4)
Deamination
(Maxwell et al.,2004)
(5)
Direct craking
Gaseous hydrocarbons
(Solomon et.al,1992)
(6)
Hydrogenation
(Solomon et.al,1992)
(7)
Hydrogenation
(Solomon et.al,1992)
(8)
(pyrolysis process in this paper)

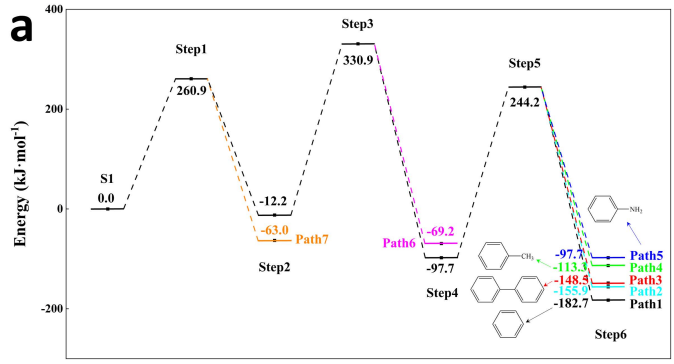
a
Energy (kJ·mol⁻¹)
400
200
0
-200
S1
0.0
Step1
260.9
-12.2
-63.0
Path7
Step2
Step3
330.9
Path6
-69.2
-97.7
Step4
Step5
244.2
-97.7
-113.3
-148.5
-155.9
-182.7
Path5
Path4
Path3
Path2
Path1
Step6

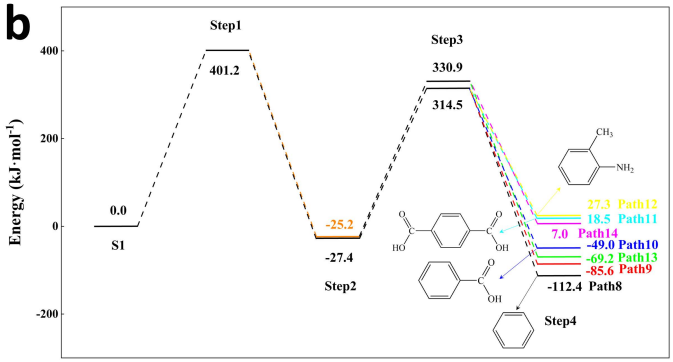
b
Energy (kJ·mol⁻¹)
400
200
0
-200
Step1
401.2
Step3
330.9
314.5
0.0
S1
-25.2
-27.4
Step2
27.3 Path12
18.5 Path11
7.0 Path14
-49.0 Path10
-69.2 Path13
-85.6 Path9
-112.4 Path8
Step4

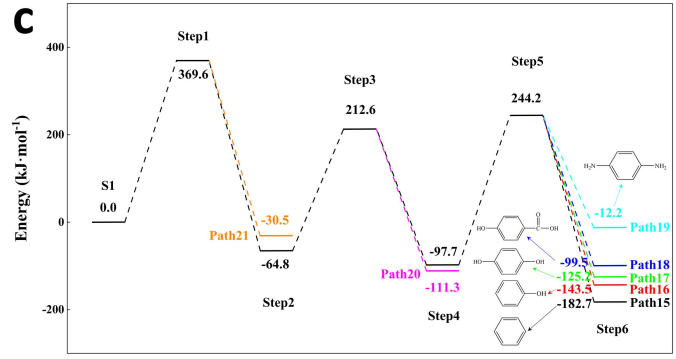
c
Energy (kJ·mol⁻¹)
400
200
0
-200
S1
0.0
Step1
369.6
-30.5
Path21
-64.8
Step2
Step3
212.6
Path20
-97.7
-111.3
Step4
Step5
244.2
-12.2
Path19
-99.5
-125.2
-143.5
-182.7
Path18
Path17
Path16
Path15
Step6

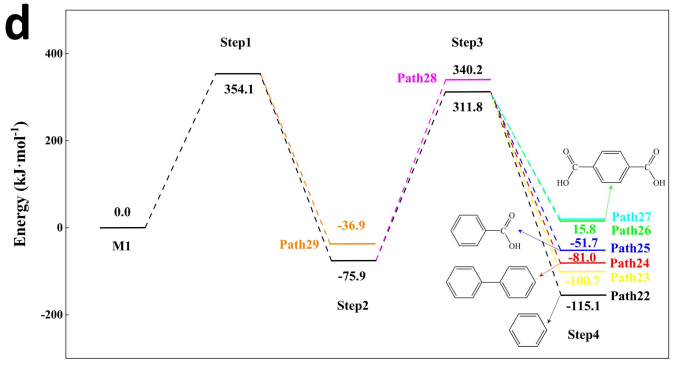
d
Energy (kJ·mol⁻¹)
400
200
0
-200
Step1
354.1
Step3
Path28
340.2
311.8
0.0
M1
-36.9
Path29
-75.9
Step2
Path27
15.8 Path26
-51.7 Path25
-81.0 Path24
-100.7 Path23
Path22
-115.1
Step4

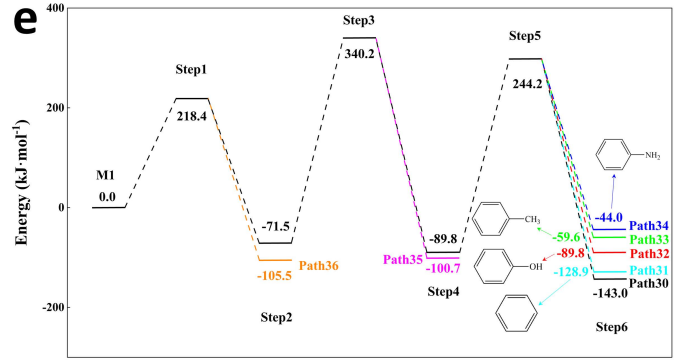
e
Energy (kJ·mol⁻¹)
400
200
0
-200
M1
0.0
Step1
218.4
-71.5
-105.5
Path36
Step2
Step3
340.2
Path35
-89.8
-100.7
Step4
Step5
244.2
-44.0
-59.6
-89.8
-128.9
-143.0
Path34
Path33
Path32
Path31
Path30
Step6

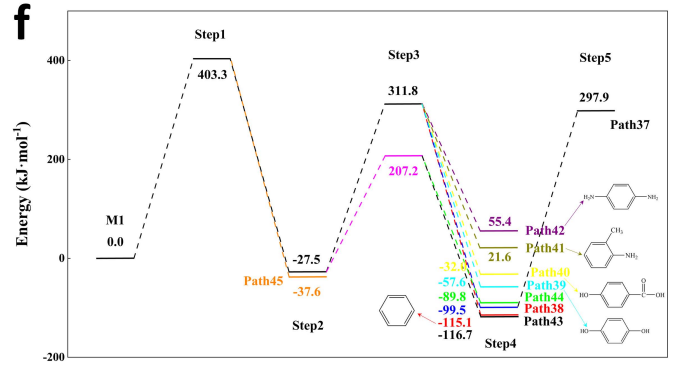
f
Energy (kJ·mol⁻¹)
400
200
0
-200
Step1
403.3
Step3
311.8
207.2
M1
0.0
-27.5
Path45
-37.6
Step2
Step5
297.9
Path37
55.4
Path42
21.6
Path41
-32.9
-57.6
-89.8
-99.5
-115.1
-116.7
Path40
Path39
Path44
Path38
Path43
Step4

Without Copper

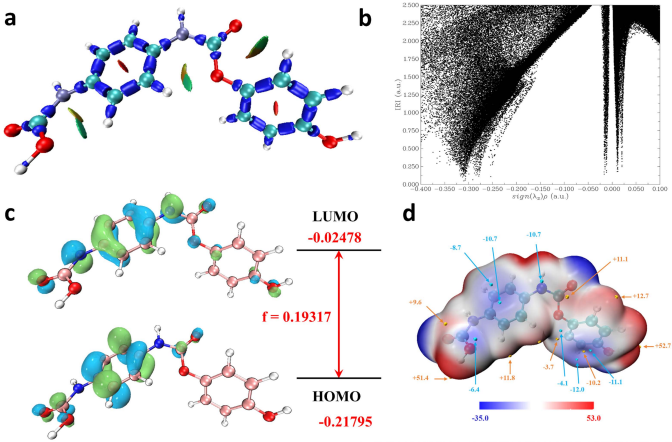

With Copper

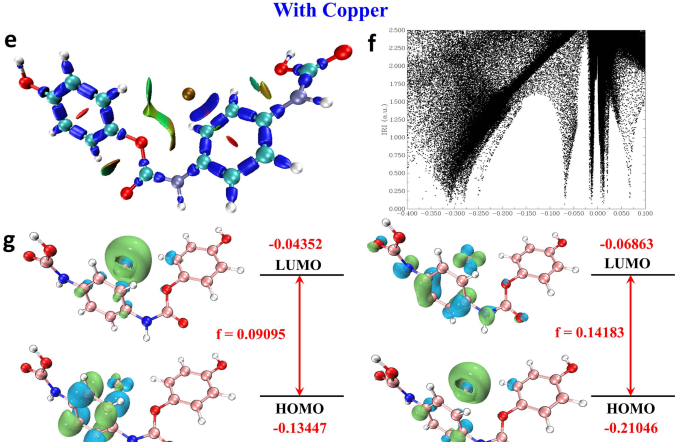

With Copper (α orbitals)

With Copper (β orbitals)

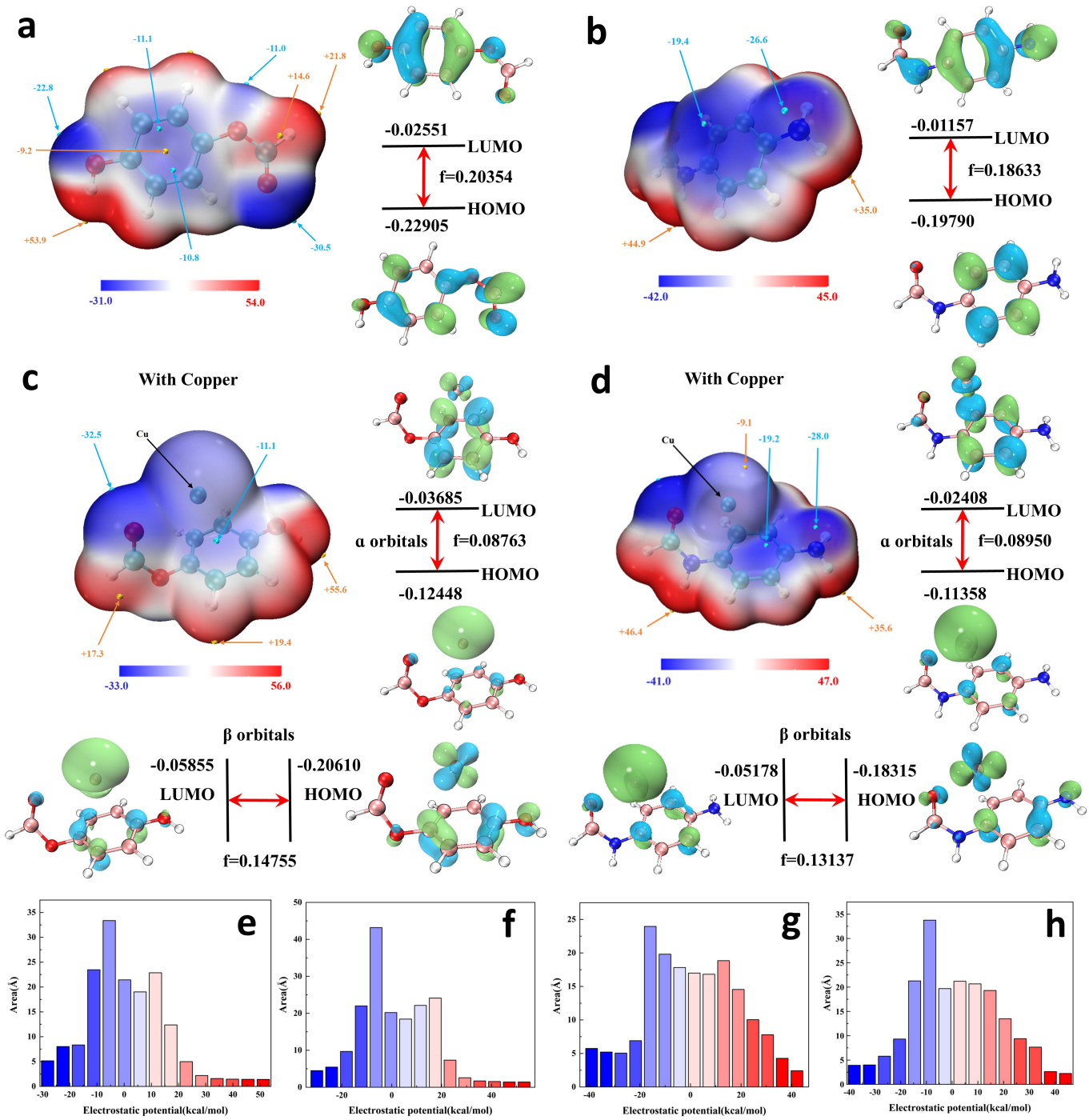
a
-11.1
-11.0
+21.8
+14.6
-22.8
-9.2
+53.9
-10.8
-30.5
-31.0
54.0
-0.02551
LUMO
f=0.20354
HOMO
-0.22905
b
-19.4
-26.6
+35.0
+44.9
-42.0
45.0
-0.01157
LUMO
f=0.18633
HOMO
-0.19790
c
With Copper
-32.5
Cu
-11.1
+55.6
+17.3
+19.4
-33.0
56.0
-0.03685
LUMO
α orbitals
f=0.08763
HOMO
-0.12448
β orbitals
-0.05855
LUMO
-0.20610
HOMO
f=0.14755
d
With Copper
-9.1
Cu
-19.2
-28.0
+46.4
+35.6
-41.0
47.0
-0.02408
LUMO
α orbitals
f=0.08950
HOMO
-0.11358
β orbitals
-0.05178
LUMO
-0.18315
HOMO
f=0.13137
e
f
g
h
Area(Å)
Electrostatic potential(kcal/mol)